Secondary electron emission and self-consistent charge transport and storage in bulk insulators: Application to alumina

X. Meyza, D. Goeuriot, C. Guerret-Piécourt, D. Tréheux, H.-J. Fitting

Secondary Electron Emission and Self-consistent Charge Transport and Storage in Bulk Insulators: Application to Alumina

X. Meyza and D. Goeuriot

Centre Sciences des Matériaux et des Structures, Ecole Nationale Supérieure des Mines, 158 cours Fauriel, 42023 Saint-Etienne cedex 2, France

C. Guerret-Piécourt *

Laboratoire de Physico-Chimie des Polymeres, UMR-CNRS 5067, Universit*é* de Pau, BP 1157, 64013 Pau cedex, France

D. Tréheux

Laboratoire d'Ingénierie et Fonctionnalisation des Surfaces, UMR-CNRS 5621, Ecole Centrale de Lyon, 36 avenue Guy de Collongue, 69134 Ecully cedex, France

H.-J. Fitting

Physics Department, University of Rostock, Universitätsplatz 3, D - 18051 Rostock, Germany

(Received

* Corresponding author:

Christelle Guerret

LPMI/CURS, BP 1155
F - 64013 Pau Cedex
FRANCE

EMail: Christelle.Guerret@univ-pau.fr
Tel: (33) 5 59 92 30 63, Fax: (33) 5 59 80 83 50

Abstract

The selfconsistent charge transport in bulk alumina samples during electron beam irradiation is described by means of an iterative computer simulation. Ballistic electron and hole transport as well as their recombination and trapping are included. As a main result the time dependent secondary electron emission rate $\sigma(t)$ and the spatial distributions of currents $j(x,t)$, charges $\rho(x,t)$, the field $F(x,t)$ and the potential slope $V(x,t)$ are obtained. For bulk insulating samples, the time-dependent distributions approach the final stationary state with $j(x,t) = \text{const} = 0$ and $\sigma = 1$. Especially for low electron beam energies $E_0 = 1$ keV, the incorporation of charges can be controlled by the potential V_G of a vacuum electrode in front of the target surface.

Finally, for high electron beam energies, the real negative surface potential $V_0 < 0$ is measured by x-ray bremsstrahlung spectra and the shift of the short wavelength edge. For the initial beam energy $E_0 = 30$ keV, the experimental value $V_0 = -16$ kV is still in good agreement with our simulations.

I. Introduction

During the last years, the influence of dielectric polarization on the essential features of dielectric and insulating materials has been investigated more intensively leading finally to better understanding and applications of these materials, see e.g. the conference series on Electric Charges in Non-Conductive Materials [1] and Ref.2. One of the subjects of interest is the prediction of electrical charging of insulators under ionizing irradiation as it is of great importance in many fields of modern technology. For instances, the knowledge of such phenomena would help in preventing insulator breakdown mainly responsible for the damage of electronic devices [3,4]. In electron microscopy like scanning electron microscopy (SEM) or Auger electron spectroscopy (AES), electron energy loss spectroscopy (EELS) etc., the prediction of the influence of charging is essential to interprete the results of analysis [5–7]. The charging of insulators has also to be known in order to manage applications such as electron lithography, electron multipliers, electrets etc. On the other hand, new problems have arisen with the deflection of interstellar dust grains in the magnetic field near the heliopause depending on their surface electric charge[8]. A great number of experimental and theoretical investigations have been published on the charging of insulators due to electron bombardment and the related secondary electron emission (SEE). Only for short pulse irradiation, target charging is prevented and the real charging-free secondary electron emission yield $\sigma(E_0)$ as a function of the primary electron energy E_0 can be measured and determined theoretically for various insulators [9–13]. However, the charging behaviour under permanent electron irradiation is not yet fully understood and the stationary final state is still very complex to describe. Indeed, the total yield approach ($\sigma \gtrless 1$) is often used to predict the sign ($\pm$) of charging in the case of stationary electron irradiation, but experimental results are not fully consistent with these predictions [14,15].

It is of importance to precise the types of theory that have been led to enlighten this phenomenon. One of the first attempts was the planar (1-dimensional) selfconsistent charging simulation of our co-author (HJF) already in 1979 [16], later on improved in Ref.17. These authors use field-dependent attenuation lengths $\lambda(F)$ for the ballistic transport of electrons and holes which had been found experimentally by means of electron beam induced currents (EBIC) measurements.

The first comprehensive Monte Carlo calculations of the self-consistent charging were made by Vicario *et al.*[18], Ganachaud *et al.*[19] and Renoud *et al.*[20]. Of course these calculations are complex because they deal with the full simulation of primary electron straggling as well as with the generation and transport of secondary electrons and holes in the selfconsistent field. Contrary to the 1-dimensional charging model based on Monte-Carlo-calculated and experimentally well-prooved attenuation lengths $\lambda(F)$ of electrons and holes, the full Monte-Carlo simulation bears more uncertainity in all the theoretical parameters used and, of course, it takes much more time for one simulation run. However, the decisive advantage of the full Monte-Carlo simulation is the 3-dimensional description of the charging process with the lateral charge spreading in case of point-like electron beam injection by a very small beam focus. Thus, the above mentioned authors[18,20] could demonstrate the build-up by a computer animation.

An approach for more rough estimation is based on the dynamic double layer model (DDLM) in which the phenomenon is brought to the simplified case of two layers of opposite charge. Complete solutions of the respective equations were achieved by Melchinger *et al.* [14]. More recently, J. Cazaux [15] developed an effective approach of the SEE evolution in insulating samples using this DDLM.

The present paper is aimed to the extension of the planar 1-dimensional self-consistent

model for thin layers as given in Refs.16,17, now to bulk insulators. It will approach full validity if the electron beam diameter is much larger than the maximum electron penetration depth $R(E_0)$. Unambiguously, this is fulfilled in scanning electron microscopes (SEM) with a slightly defocused beam. Thus the 1-dimensional simulation can be applied to 3-dimensional description of the sample potential in a SEM chamber[21]. The results will be presented in particular for alumina but could be easily adapted to any insulator using the relevant material data available in the literature.

II. Theoretical Background

The strong charging of insulators under electron beam irradiation is well known, at least, since Malter 1936 discovered the anomalous high secondary electron emission (SEE) and long-lasting electron post-emission from MgO layers[22]. A strong positive charging due to the emission of secondary electrons (SE) from the surface-near regions is responsible for that selfconsistent field-enhanced SEE. On the other hand, the deeper injection of primary electrons (PE) will produce an electron surplus within the bulk of an insulator. The respective charge $\rho(x)$ and field $\boldsymbol{F}(x)$ distributions maintain the selfconsistent charge transport and the SEE emission.

A. Generation of currents and charges

Thus, we should first refer to the injection of primary electrons (PE) and their creation of secondary electrons (SE) and holes (H). This process for Al_2O_3 is similar to that of SiO_2 as we have described already in [16,17] based on empirical results of the electron penetration process into solids having been obtained by the "film-bulk method" [23]. By means of this method the resulting PE current in dependence on the target depth x and the PE initial

energie E_0 was found:

$$j_{\mathrm{PE}}(x, E_0) = j_0(1-\eta)\exp\left[-4.605\left(\frac{x}{R(E_0, z)}\right)^{p(z)}\right], \tag{1}$$

with j_0 as impinging PE current density and the material parameters for SiO_2: $\eta \approx 0.2$ the backscattering coefficient, $p \approx 2$ the exponential transmission parameter and the empirical equation for the maximum electron range R reached by 1% of PE:

$$R/\mathrm{nm} = \frac{900}{\rho^{0.8}}(E_0/\mathrm{keV})^{1.3} \quad \text{, for} \quad E_0 < 8\mathrm{keV} \tag{2a}$$

$$R/\mathrm{nm} = \frac{450}{\rho^{0.9}}(E_0/\mathrm{keV})^{1.7} \quad \text{, for} \quad E_0 \geq 8\mathrm{keV} \tag{2b}$$

R is given in nm, the target mass density ρ in g/cm^3, and the electron beam energy E_0 in keV. In Ref.23 one can find the respective quantities of any material when knowing the mass density and the PE backscattering ratio $\eta(E_0)$.

The generation rate $g_i(x, E_0)$ of inner secondary electrons (SE) is proportional to the spatial energy loss dE/dx of the impinging and straggling primary electrons (PE), i.e. proportional to the spatial PE energy transfer to the target volume:

$$g_i(x, E_0) = \alpha \, \frac{1}{E_i} \, \frac{dE}{dx}, \tag{3}$$

where E_i is the mean creation energy for one SE and α a yield factor of nearly a unit. According to Klein[24] and Alig and Bloom[25] the SE creation energy increases with the energy gap E_g of a given target material

$$E_i \approx 3E_g + 1\mathrm{eV} \tag{4}$$

resulting in $E_i \approx 28$ eV for Al_2O_3 with $E_g = 9$ eV. Then with Eq.(3) and empirical expressions for dE/dx from Ref.23, we may write the SE creation rate in Al_2O_3 in the

form of a semi-empirical equation

$$g_i/\mathring{A} = 0.146(E_0/\mathrm{keV})^{-0.3} \exp\left[-7.5\left(\frac{x}{R} - 0.3\right)^2\right]. \tag{5}$$

This is a Gaussian distribution with the maximum shifted by $0.3R$ from the surface into the target volume. Assuming an isotropic SE generation, one half of the created SE: $1/2 j_0 g_i(x, E_0)\Delta x$ will move into the bulk sample, i.e. in the direction towards the sample support and the other half towards the sample surface. Then the respective continuity equation in 1-dimensional form for any SE or hole currents in transmission (T) direction towards the sample substrate (holder) or in reverse (R) direction towards the surface looks very simple:

$$j_T^R(x) = \left[j_T^R(x \pm \Delta x) + \frac{1}{2} j_0 g_i(x)\Delta x\right] W(x) \tag{6}$$

with the first term in the brackets for the convection part and the second one for the generation of inner SE or holes followed by the overall attenuation probability $W(x)$ of the charge carriers over the small distance Δx in the target depth x. This attenuation probability will be described separately below.

Thus the current possesses sources with $g_i(x)$ as well as drains due to the attenuation $W(x)$. Introducing the excessive charge $\Delta\rho$ into the continuity equation we get for the actual charge change over the time Δt in the depth Δx and for the time t:

$$\Delta\rho(x,t) = -\frac{j(x+\Delta x,t) - j(x-\Delta x,t)}{2\Delta x} \cdot \Delta t \tag{7a}$$

Adding this excessive charge $\Delta\rho$ to the already present charge:

$$\rho(x,t) = \rho(x, t-\Delta t) + \Delta\rho(x,t) \tag{7b}$$

we may obtain the electrical field distribution $F(x)$ via the Poisson equation, i.e. by integration of the charges:

$$F(x,t) = \frac{1}{\varepsilon_0 \varepsilon_r} \int_0^x \rho(x',t)dx' \tag{8}$$

Further on, the related potential slope $V(x,t)$ is given by

$$V(x,t) = \int_d^x F(x',t)dx' \tag{9}$$

Because the sample support should be grounded, $V(x=d)=0$, the integration starts at the sample support electrode in the depth d denoting the sample surface with $x=0$ and the back electrode with the target thickness $x=d$.

B. Attenuation of currents

In context with Eq.(6) we have introduced the overall attenuation probability W. First of all W will depend on the actual field strength F enhancing or diminishing the mean attenuation length $\lambda(F)$. This very important transport parameter has been investigated experimentally[26,27] as well as calculated by Monte Carlo simulations[28–30].

Thus the field-dependent attenuation probability indicated for electrons by (E) in transmission (T) and reverse (R) direction is:

$${}^{R}_{T}W_{EF} = \exp\left[-\frac{\Delta x}{\lambda_E(\pm F)}\right] = \exp\left[-\frac{\Delta x}{\lambda_{E,0}\,\exp(\pm\beta_E F)}\right] \tag{10a}$$

For holes (H) we can write the respective relation:

$${}^{R}_{T}W_{HF} = \exp\left[-\frac{\Delta x}{\lambda_H(\mp F)}\right] = \exp\left[-\frac{\Delta x}{\lambda_{H,0}\,\exp(\mp\beta_H F)}\right] \tag{10b}$$

including the mean field-dependent attenuation length λ_E for electrons and λ_H for holes with their field-free values $\lambda_{E,0}$ and $\lambda_{H,0}$ as well as the field-enhancing factors β_E and β_H, respectively.

Whereas the mean attenuation length for electrons $\lambda_E(\pm F)$ is enhanced for positive fields

$F > 0$ in reverse (R) motion towards the surface, it is diminished for transmission (T) direction towards the sample support. Negative fields $F < 0$ will result in opposite relations for electrons, i.e. enhancement in (T) and retarding in (R) direction, respectively. Of course, for holes (H) the relations for ${}^{R}_{T}W_{HF}$ in Eq.(10b) should be given vice versa, i.e. with an opposite sign with respect to electrons in Eq.(10a).

Further on, we should consider electron-hole recombination as a second kind of current attenuation. With the related recombination cross sections $S_{EH} = S_{HE}$, we can write the recombination probability for electrons over the distance Δx:

$$W_{EH} = \exp\left[-\frac{\rho_H}{e_0} S_{EH} \Delta x\right] \tag{11a}$$

as well as for holes:

$$W_{HE} = \exp\left[-\frac{\rho_E}{e_0} S_{HE} \Delta x\right] \tag{11b}$$

Now the charges are required separately for electrons ρ_E and for holes ρ_H, respectively. Another attenuation of the currents is given by the trapping probability to localized electron states (traps) with an overall concentration $N_{E,0}$ and an actual occupation N_E:

$$W_{EE} = \exp\left\{-[N_{E,0} - N_E(x)]\ S_{EE} \Delta x\right\} \tag{12a}$$

$N_{H,0}$ and N_H denote for hole concentrations, respectively:

$$W_{HH} = \exp\left\{-[N_{H,0} - N_H(x)]\ S_{HH} \Delta x\right\} \tag{12b}$$

S_{EE} and S_{HH} hold for the capture cross sections for electrons and holes, respectively. Finally we can write the current of Eq.(6) explicitely for electrons (E) in reverse (R) and transmission (T) direction

$$j^{ER}_{ET}(x) = \left[j^{ER}_{ET}(x \pm \Delta x) + \frac{1}{2} j_0 g_i(x) \Delta x\right] {}^{R}_{T}W_{EF} \cdot W_{EH} \cdot W_{EE} \tag{13a}$$

as well as for holes (H):

$$j_{HT}^{HR}(x) = \left[j_{HT}^{HR}(x \pm \Delta x) + \frac{1}{2} j_0 g_i(x) \Delta x \right] {}_{T}^{R}W_{HF} \cdot W_{HE} \cdot W_{HH} \tag{13b}$$

with the respective expressions for the different kinds of attenuation from Eqs.(10) - (12). The overall current $j(x)$ in the depth x is given by summation of the several components of Eqs.(1), (13a), and (13b).

$$j(x) = -j_{PE}(x) - j_{ET}(x) + j_{ER}(x) + j_{HT}(x) - j_{HR}(x) \tag{14}$$

resulting in the positive sign for positive charges moving in x-direction, i.e. transmission. This current can be inserted into the continuity Eq.(7), providing the excessive charge $\Delta\rho(x)$ as well as via Eq.(8) the respective field distribution $F(x)$, and the potential slope $V(x)$ by means of Eq.(9).

III. Simulation of the Charging Process

The simulation procedure should be oriented to real experimental conditions. In Fig.1 the scheme of a secondary electron microscope (SEM) chamber is presented showing the respective currents of primary electrons I_0, of the total secondary emission σI_0 with $\sigma = \eta + \delta$ as the sum of backscattered BE (η) and true SE (δ) released from the target material.

A certain part of emitted electrons can be backscattered or re-emitted from the microscope chamber or from a negatively biased electronic grid. These electrons are called tertiary electrons TE.

The insulating target, of course, allows three currents to the grounded support: an instationary displacement current of polarization I_P, a real conduction current I_C through the bulk to the metallic support as well as a surface leakage current I_S. In their sum they are

forming the overall target support current I_M:

$$I_M = I_P + I_C + I_S \tag{15}$$

The directions of the injected PE current j_{PE}, the inner secondary electron (SE) current j_{SE} and the respective hole current j_H are schematically presented in Fig.2. However, in our case of a bulk Al_2O_3 target, the relatively large thickness of $d = 3$ mm will not allow neither a real conduction current j_C to the support nor a Fowler-Nordheim tunneling injection current j_{FN} from the metallic support into the insulator. The latter one appears only for thin layers $d < 300$ nm and $\sigma > 1$ connected with strong positive charging, see [16,17].

On the other hand, at the surface barrier with an electron affinity χ a certain fraction P_S of incident inner secondary electrons with an energy $\overline{E}_{SE}$ will be reflected: $P_S = \sqrt{\chi/\ \overline{E}_{SE}}$; the other part $P_{SE} = 1 - \sqrt{\chi/\ \overline{E}_{SE}}$ is emitted as secondary electrons over the surface barrier into the vacuum [31]. For Al_2O_3 with $\chi \simeq 0.9$ eV and $\overline{E}_{SE} \approx 6$ eV we get $P_S \simeq 0.39$ for the surface reflection coefficient and $P_{SE} = 0.61$ for the SE emission probability.

Furthermore, in the presence of a screening or retarding grid or any vacuum electrode, even, by the SEM chamber itself, biased to a potential V_G less than the actual surface potential $V_0 = V(x = 0)$ of the sample surface, i.e. only for $V_G < V_0$, we observe a SE retarding field current reverse to the surface of a rate

$$P_G = 1 - \exp \frac{V_G - V_0}{V_{SE}} \tag{16}$$

as already introduced in Refs.16,17. With Eq.(16) and $e_0 V_{SE} \approx 5$ eV as the mean kinetic energy of emitted SE, we may characterize the retarding field curve of SE.

Thus we get the boundary conditions of the SE current at the surface $x = 0$ with the

possibility of twofold reflection at the surface with P_S and at the negative grid with P_G:

$$j_{ET}(x=0) \quad = \quad j_{ER}(x=0)\,[P_S + (1-P_S)P_G] \tag{17}$$

These both reflections of reverse (R) moving electrons at the surface and at a retarding electrode are indicated with TE (tertiary electrons) in Fig.2. Further on, we should assume that holes are reflected entirely at the surface barrier. So we get:

$$j_{HT}(x=0) \quad = \quad j_{HR}(x=0) \tag{18}$$

When calculating the current balance across the layer according Eqs.(13a) and (13b), we always have to start with the reverse current j_R at its beginning in the volume behind the maximum excitation depth $R(E_0)$, then going towards the surface and starting the transmission current j_T with the reflection parts of j_R at the surface, see Eq.(17).

After summing up all currents $j(x,t)$ over all x for a certain time t according Eq.(14), we should calculate the respective charges $\rho(x,t)$, fields $F(x,t)$ and potentials $V(x,t)$ as given by Eqs.(7)-(9). Then we repeat this procedure in an iteration cycle till we get a stationary-like state for the actual irradiation time t. Afterwards we increase t by Δt and repeat the iteration cycle. The final stationary irradiation state in an insulator is reached when no changes of the overall current along x are observed, i.e. $j(x,t) = \text{const}$, or div $\boldsymbol{j} = 0$. Then also the charge, field, and potential distributions are not changing anymore with time. All is in a stationary equilibrium, in the final steady state.

IV. Computational Results

The simulations of the self-consistent charge transport were performed for 3 mm thick alumina samples by means of the material parameters given in Tab.1 with their references extended by [32–39]. We look first to the positive charging at a low electron beam energy

$E_0 = 1$ keV, presented in Fig.3. There we see the time evolution of the current $j(x,t)$ as well as the respective charge $\rho(x,t)$ and field $F(x,t)$ distributions. Obviously we obtain a suppression of the currents $j(x,t)$ with time t, Fig.3(a), caused by retarding and re-injection of SE due to a positively charged sample surface with respect to the grounded grid $V_G = 0$. This process has been described in context with Eq.(17). The resulting emission current $j(x < 0)$ becomes zero and the SE rate approaches $\sigma = 1$. Thus the SEE is blocked and the positive charging becomes stable after about 50 ms, see Fig.3(b). Due to re-injected secondary electrons the charge distribution shows a minus-plus-minus structure. However, the positive charges are only slightly prevailing the negative ones leading to a relatively small positive surface potential $V_0 \simeq +4.34$ V, (as we will see later on in Fig.6(a)), and an almost zero field strength towards the sample support, Fig.3(c).

A contrary behavior we find for a high electron beam energy and related negative charging. In Fig.4, the respective current $j(x,t)$, charge $\rho(x,t)$, and field $F(x,t)$ distributions are presented for an initial beam energy $E_0 = 30$ keV. Very obviously, with increasing time t the overall current $j(x,t)$ is more and more restricted to surface-near regions. Finally, in the stationary state $j(x,t) = \text{const} = 0$ the irradiation depth has decreased from 4.5 μm at the beginning $t = 0$ to about 0.8 μm for $t > 100$ ms, Fig.4(a). Looking to the incorporated charge distribution $\rho(x,t)$ (Fig.4(b)) we recognize strongly prevailing negative charges correlated with negative field strengths over the bulk volume $x > 1\mu$m, Fig.4(c). Due to secondary electron emission (SEE) into vacuum from a mean escape depth of $\lambda_{E0} = 5$ nm beneath the surface of the insulator the charge distribution in this zone indicates an electron deficit, i.e. positive charge storage, as we see in Fig.5, which has been zoomed to nm scale presentation. Nevertheless, the surface potential $V_0(x \to 0)$ in this region approaches high negative values of about $V_0 \simeq -22$ kV, Fig.6(b). Of course,

this negative surface potential is responsible for the electron beam decelleration from originally $E_0 = 30$ keV down to only $E_0' \simeq 8$ keV. Indeed, this diminishes the irradiation depth zone as we see in Fig.4(a).

Moreover, because of the positive surface charge, there is a small potential decay for electrons towards the surface, maintaining an enhanced SEE and leading finally to the stationary steady state with $\sigma = \eta + \delta = 1$ and the overall current $j(x,t) = 0$ over the entire volume and for all times $t \geq 100$ ms.

V. Discussion

From the current $j(x,t)$ and potential $V(x,t)$ distributions of the previous part, we may deduce the respective secondary electron (SE) emission rate $\sigma(t)$ as well as the surface potential $V_0(t) = V(x{=}0,t)$. Both quantities are accessible from outside the sample and can be proved directly by measurements, Fitting[16].

The SE rate is given by

$$\sigma = \eta + \delta = \frac{I_{BE} + I_{SE}}{I_0} = \frac{I_0 + I(x<0)}{I_0} = 1 + \frac{I(x<0)}{I_0} \tag{19}$$

where $I(x<0)$ is the "resulting" electron current into the vacuum diminished, of course, by the impinging reverse moving PE beam current I_0. So we have to add again I_0 to $I(x<0)$ in order to get the real emission current $(I_{BE} + I_{SE})$ and the respective fractions $(\eta + \delta)$.

We may observe the time dependence of the surface potential $V_0(t)$ and the secondary emission $\sigma(t)$ presented in Fig.6 and Fig.7, respectively.

As we have already mentioned the positive charging at $E_0 = 1$ keV is limited by the grounded surrounding (grid potential $V_G = 0$). So V_0 passes a maximum of $V_0 = +4.6$ V after $t \approx 5$ ms and is then decaying to about $V_0 = +4.35$ V for times $t > 30$ ms. On the

other hand, the negative charging at $E_0 = 30$ keV is not limited by returning SE (or TE), even SE are enforced to leave the negative surface, and the surface potential approaches a saturation with $V_0 \approx -21$ kV after $t \geq 20$ ms. Of course, this huge negative charging has led to a retarding of the primary electron beam. This retarding of incident PE is correlated with a decrease of the maximum electron range $R(E_0')$ within the insulating sample.

In Fig.7 the time-dependent SE rates $\sigma(t)$ are presented. Clearly we recognize the blocked SEE to $\sigma = 1$ for $E_0 = 1$ keV after 1 μs as well as the increase of SEE for $E_0 = 30$ keV. The latter one is caused by PE retarding due to the negative surface potential $V_0 < 0$ and, consequently, by a higher SE rate $\sigma(E_0')$. Because the backscattering (BE) fraction of Al_2O_3 with $\eta \simeq 0.18$ is nearly constant the true SE rate $\delta_0(E_0 = 30\text{keV}, t = 0) = 0.35$ has increased to $\delta(E_0' \simeq 8\text{keV}, t > 20\text{ms}) \approx 0.82$. Indeed, this is a drastic change of the SE emission rate due to the negative charging within the insulators. The steady state $\sigma = 1$ is obtained after about 25 ms.

Let us now investigate the influence of the grid potential V_G (hitherto we have considered only $V_G = 0$). In Fig.7 we see a drastic change of the σ-slope with time when increasing the grid potential V_G to +10 V; + 100 V, and + 1000 V. Now, obviously, the surface will be charged more positively and it takes more time until the surface potential V_0 is reaching the positive grid potential V_G and starting the retarding process according to Eq.(16) will set on.

Indeed, when looking to the time-dependent and final steady state charge distributions in Figs.(8a) and (8b), respectively, we see that the grid potential considerably controls the incorporated charge. For high grid voltages $V_G = +1000$ V, even we get a plus-minus-plus-minus charge distribution instead of a minus-plus-minus one obtaines for lower V_G.

Also the range of incorporated charges is increasing with V_G. That indicates that the surface potential V_0 has become more positive and the incident beam energy is increased by $+eV_0$.

Generally we may state that the actual retarded or elevated electron beam energy E_0' is diminished or increases by the surface potential V_0

$$E_0' = E_0 + eV_0 \tag{20}$$

Thus, in Fig.9 we have plotted the maximum range R versus the initial beam energy E_0 as given in Eqs.(2a) and (2b) and have compared it with the resulting actual range $R(E_0')$ obtained in the final steady state of irradiation, i.e. in the case of $E_0 = 30$ keV after $t > 25$ ms. Obviously, the observed value $R(E_0') \simeq 0.9\mu$m corresponds to an actual retarded or enhanced beam energy $E_0' \simeq 9$ keV according to Eq.(20). Of course, this value is expected from the surface potential $V_0 = -21$ kV in context with Eqs.(20) and (2b).

Then let us check the other accessible quantity, the SE rate σ. In Fig.10 we have plotted the initial SE rate $\sigma_0(E_0) = \sigma(E_0, t = 0)$, i.e. the real material-dependent SE rate from fresh and non-charged samples. With our calculations we obtain a maximum of the SE rate $\sigma_0(E_0 = 0.7\text{keV}) = 2.4$. This corresponds approximately to the experimental values presented by Seiler[10] with $\sigma_{\max} = 2.6 - 4.7$, but it is considerably smaller than the maximum value $\sigma_{\max} \approx 6.4$ of Dawson[40]. The first sigma-unit point is found with $\sigma_0(E_0^I = 50\text{eV}) = 1$ and the second one at $\sigma_0(E_0^{II} = 8.4\text{keV}) = 1$.

Further on, in case of thick insulating samples the SE rate will approach very rapidly the steady state with $\sigma = 1$. We see in Figs.9 and 10 that the negative charging for high beam energies $E_0 = 30$ keV never will approach so high values that the retarded electron range $R(E_0')$ would be comparable with the SE maximum escape depth of about 25 nm as predicted by the Cazaux model[7]. This point is related to the fact, that the slowing-down

of the electrons is mostly due to the negative surface voltage and less to an inner slowing-down as described by J. Cazaux. Moreover, the retarded energy $E_0' = 9$ keV approaches almost the second sigma-unit point $E_0'' = 8.4$ keV and the conventional bipolar model is nearly fulfilled.

On the other hand, for low beam energies $E_0 = 1$ keV and positive charging $V_0 > 0$, the initial SE rate $\sigma_0 > 1$ will be suppressed very rapidly down to $\sigma = 1$ by a grounded vacuum electrode or grid biased to $V_G = 0$. So the surface potential approaches only small positive values of $V_0 \approx +(4...5)$ eV as we have seen also in Fig.6(a). But increasing the voltage potential to $V_G = +1000$ V, $\sigma(E_0)$ follows the surface potential up to $V_0 = +1002$ V, i.e. to $E_0' = 2002$ eV, and drops then rapidly to the final steady state $\sigma = 1$. Also here the bipolar model in its tendency is fulfilled but the positive charging is limited again by the controlling grid voltage V_G.

In order to prove the accessible quantities $V_0(t)$ and $\sigma(t)$, we have chosen two experiments. The first one is measuring the surface potential V_0 by means of the x-ray bremsstrahlung (BS) spectra, i.e. by the shift of the short wavelength threshold due to the negative surface potential V_0 and respective retarding of the PE beam according to Eq.(20). This method has been proposed already by other authors, e.g. in Belhaj *et al.*[6]. In Fig.11 this effect is demonstrated for the 3mm Al_2O_3 sample and $E_0 = 30$ keV electron beam irradiation. We observe the BS short wave limit at $E_x = 13$ keV; that corresponds to a negative surface potential of $V_0^{\exp} = -17$ kV. Comparing this with our simulation value of $V_0 = -21$ kV from Fig.6 and Fig.10 we recognize a worse isolation behavior of the real experimental Al_2O_3 target than of the simulated one. Indeed, this was expected and, nevertheless, it demonstrates the right tendency of huge negative charging of thick insulating samples under high energy electron beam irradiation with $\sigma_0(E_0) < 1$. Concerning the second

accessible quantity $\sigma(t)$, it can be deduced from the measurement of the overall target support current I_M[21]. These results will be detailled elsewhere.

VI. Conclusions

The one-dimensional approach of ballistic electron and hole transport allows to simulate the self-consistent charging-up process in bulk insulators. Because of the great thickness of the insulating samples, the surface potential V_0 changes very rapidly and is controlling the further incorporation of charges. At high electron beam energies $E_0 = 30$ keV the surface potential becomes strongly negative and the electron beam is decellerated down to $E_0' = E_0 + eV_0 \approx 9$ keV near to the second sigma-unit value $\sigma(E_0^{II} = 8.4\text{keV}) = 1$. Thus the bipolar model of opposite charging is nearly fulfilled. On the other hand, the charge beneath the surface is positive because of the favoured SE escape and we obtain a plus-minus-plus-minus spatial charge structure with prevailing minus parts within the bulk insulator.

For low energy electron bombardment $E_0 \approx 1$ keV the rapid positive charging suppresses a field-enhanced SE escape and the steady state with $j(x,t) = \text{const} = 0 \quad \text{and} \quad \sigma = 1$ produces a minus-plus-minus charge distribution. Now the surface potential is only weakly positive and exceeds that of the grounded SEM chamber ($V_G = 0$) only by $V_0 = +4.5$ V. But for higher grid potentials V_G up to + 1000 V and $E_0 = 1$ keV the positive charging is much greater and approaches $V_0 \simeq V_G$. Thus the beam energy amounts $E_0' = E_0 + eV_G$ and tries to approach the second sigma-unit point E_0^{II}. Here the bipolar model also becomes valid.

The experimental methods of the bremsstrahlung shift allows us to measure the surface potential V_0. The experimental result is still in a sufficient agreement with our selfconsis-

tent simulation of the charging process.

Acknowledgement

The authors wish to acknowledge D. Juvé for valuable measurements and G. Damamme for fruitful discussions.

References

[1] 4th International Conference on Electric Charges in Non-Conductive Materials, Le Vide: Science, Techniques et Applications, Vol. Special CSC'4, 2001

[2] G. Blaise, W. J. Sarjeant, IEEE Transactions on Dielectrics and Electrical Insulation, **5**, 779 (1998)

[3] L. Levy, Space Technology Course, Cepadues Editions 2002, Toulouse, France, pp. 241

[4] V. Griseri, L. Levy, D. Payan, T. Maeno, K. Fukunaga, C. Laurent, Annual Report: Conference on Electrical Insulation and Dielectric Phenomena, Omni-Press, Piscataway, USA, 2002, pp. 922

[5] J. Cazaux, J. of Electron Spectroscopy, **105**, 155 (1999)

[6] M. Belhaj, O. Ibara, M. N. Filippov, E. I. Rau, M. V. Andrianov, Appl. Surf. Sci **177**, 58 (2001)

[7] J. Cazaux, J. Appl. Phys. **89**, 8265 (2001)

[8] H. Kimura, I. Mann, Earths Planets Space **51**, 1223 (1999)

[9] O. Hachenberg, W. Brauer, Adv. Electronics **11**, 413 (1959)

[10] H. Seiler, Z. Angew. Phys. **22**, 249 (1967)

[11] P. H. Dawson, J. Appl. Phys. **37**, 3644 (1966)

[12] L. Reimer, Scanning Electron Microscopy, Springer Series in Optical Sciences (Berlin) **45** (1985)

[13] O. Hachenberg, W. Brauer, Scanning Microscopy **4**, 57 (1990)

[14] A. Melchinger, S. Hofmann, J. Appl. Phys. **78**, 6624 (1995)

[15] J. Cazaux, J. Appl. Phys. **85**, 1137 (1999)

[16] H.-J. Fitting, H. Glaefeke, W. Wild, M. Franke, W. Müller, Exp. Tech. Phys. **27**, 13 (1979)

[17] I. A. Glavatskikh, V. S. Kortov, H.-J. Fitting, J. Appl. Phys. **89**, 440 (2001)

[18] E. Vicario, N. Rosenberg, R. Renoud, Surface and Interface Analysis **22**, 115 (1994)

[19] J. P. Ganachaud, C. Attard, R. Renoud, Physica Status Solidi (b) **199**, 175 and 455 (1997)

[20] R. Renoud, F. Mady, J. P. Ganachaud, J. Phys.: Condensed Matter **14**, 231 (2002)

[21] X. Meyza, PhD thesis, Ecole Superieure des Mines de Saint-Etienne, 2003

[22] L. Malter, Phys. Rev. **49**, 478 (1936)

[23] H.-J. Fitting, H. Glaefeke, W. Wild, Phys. Status Solidi (a) **43**, 185 (1977)

[24] C. A. Klein, J. Appl. Phys. **39**, 2029 (1968)

[25] R. C. Alig, S. Bloom, Phys. Rev. Lett. **35**, 1522 (1975)

[26] H.-J. Fitting, H. Glaefeke, W. Wild, R. Ulbricht, Exp. Tech. Phys. (Berlin) **24**, 447 (1976)

[27] Th. Hingst, M. Hübner, R. Franz, Ch. Kuhr, H.-J. Fitting, Microelectronic Eng. **24**, 181 (1994)

[28] H.-J. Fitting, J.-U. Friemann, Phys. Status Solidi (a) **69**, 349 (1982)

[29] H.-J. Fitting, J. Boyde, Phys. Status Solidi (a) **75**, 137 (1983)

[30] E. Schreiber, H.-J. Fitting,
J. Electron Spectroscopy & Related Phenomena **124**, 25 (2002)

[31] H.-J. Fitting, H. Glaefeke, W. Wild, Surface Sci. **75**, 267 (1978)

[32] D. Dew-Hughes and O. H. Wyatt, in: Metals, Ceramics and Polymers,
Cambridge University Press, New York 1974

[33] D. R. Lide, in: Handbook of Chemistry and Physics, 83rd Edition,
CRC Press 2001, Gaithersburg/Maryland

[34] W. H. Strehlow and E. L. Cook, J. Phys. Chem. **2**, 163 (1973)

[35] A. H. Sommer, in: Photoemission Materials, Wiley ed. New York (1968)

[36] T. H. Ning, J. Appl. Phys. **47**, 3203 (1976)

[37] I. I. Milman, V. S. Kortov, S. V. Nikiforov,
Radiation Measurements **29**, 401 (1998)

[38] V. A. J. Van Lint, J. M. Bunch, T. M. Flanagan, Proceedings of the Conference
on Radiation Effects and Tritium Technology for Fusion Reactors, vol. **11**, pp. 531
ed. by J. S. Watson, F. W. Wiffen, I. L. Bishop, B. K. Breeden, Gatlinburg/Tennessee,
1976

[39] P. C. Srivasta, A. Roy Bardhan, D. L. Bhattacharya,
Intern. J. Electronics **46**, 547 (1979)

[40] P. H. Dawson, J. Appl. Phys. **37**, 3644 (1966)

Captions for the Figures

Fig. 1 Electron irradiation of an insulating target in a scanning electron microscope (SEM): I_0 - incident PE current, σI_0 - backscattered (BE) and secondary (SE) part, I_{TE} - tertiary electrons backscattered from the chamber, I_S - surface leakage current, I_C - real conduction current, I_P - instationary displacement current due to charge trapping and incorporation, I_M sample stage current.

Fig. 2 Scheme of currents in an insulating sample of thickness d during electron irradiation with primary electrons (PE). The currents of inner secondary electrons (SE) and holes (H) are given in foreward (T: transmission) and in reverse (R) direction, see Eq.(13). The total re-emission fraction $\sigma = \eta + \delta$ of backscattered electrons (BE) and SE is diminished by tertiary electrons (TE)

Fig. 3 Low energy $E_0 = 1$ keV electron irradiation and the related evolution a) of internal currents j, b) charge distributions ρ, and c) field F; incident current density $j_0 = 10^{-5}$ A/cm^2.

Fig. 4 High energy $E_0 = 30$ keV electron irradiation and the related evolution of a) internal currents j, b) charge distributions ρ, and c) field F; incident current density $j_0 = 10^{-5}$ A/cm^2.

Fig. 5 Positively charged surface region due to forced SE escape in spite of high PE energy $E_0 = 30$ keV, but due to an overall negative repulsing charge; zoomed in nm scale.

Fig. 6 Surface potential V_0 as a function of the irradiation time t ; with beam energies a) $E_0 = 1$ keV and b) 30 keV, and incident current densities $j_0 = 10^{-5}$ A/cm^2, please note the different voltage scales in V and kV.

Fig. 7 Rapid change of the secondary electron emission fraction $\sigma = \eta + \delta$ with irradiation time t for $E_0 = 1$ keV and 30 keV, respectively, and different vacuum grid potentials V_G. The initial value $\sigma_0(t \to 0)$ corresponds to the non-charged Al_2O_3 sample; the final steady state for the bulk sample ($d = 3$ mm) should always approach $\sigma = 1$; ($j_0 = 10^{-5}$ A/cm^2).

Fig. 8 Charge distributions $\rho(x)$ for a low energy injection $E_0 = 1$ keV and different vacuum grid potentials V_G, a) in dependence on irradiation time for $V_G = +1000$ V ; b) final steady state distributions for different V_G.

Fig. 9 Maximum range $R(E_0)$ of primary electrons in non-charged Al_2O_3 targets (o) retarded by negative charging at $E_0 = 30$ keV to a much lower value $E_0' \simeq 9$ keV (•) as well as accellerated at $E_0 = 1$ keV and $V_G = +1000$ V to $E_0' \simeq 2000$ keV (•).

Fig. 10 Initial rate (o) of secondary electrons $\sigma_0(E_0)$ from Al_2O_3 as a function of the PE energy E_0 as well as its change by charging to $\sigma(E_0')$ (•) (in context with Eq.(20)); sample thickness $d = 3$ mm.

Fig. 11 Measurement of the negative surface potential V_0 by means of the EDX bremsstrahlung (BS) threshold shift: $E_x' = E_0 + eV_0 = E_0'$, initial beam energy $E_0 = 30$ keV.

TABLE I. Material parameters of Al_2O_3 used in the present simulation

Al_2O_3 material parameters	**Unit**	**Value**	**Symbol**	**References**
Mass density	(g/cm^3)	3.98	ρ	
Electrical permittivity		10	ϵ_r	32-33
Energy band gap	(eV)	9	E_g	34
Mean ionization energy	(eV)	28	E_i	23-24
Electron affinity	(eV)	0.9	χ	35
SE mean attenuation length	(nm)	5	$\lambda_{E,0}$	16
Hole mean attenuation length	(nm)	2	$\lambda_{H,0}$	16
SE attenuation field factor	(cm/MV)	4.6	β_E	16
Hole attenuation field factor	(cm/MV)	0.8	β_H	16
e-h-recombination cross section	(10^{-13} cm^2)	1	$S_{EH} = S_{HE}$	36
Concentration of electron traps	(10^{17} cm^{-3})	1-5	$N_{E,0}$	20, 37-39
Concentration of hole traps		not considered	$N_{H,0}$	
Trapping cross section of electrons	(10^{-15} cm^2)	1	S_{EE}	20, 37-39
Trapping cross section of holes		not considered	S_{HH}	

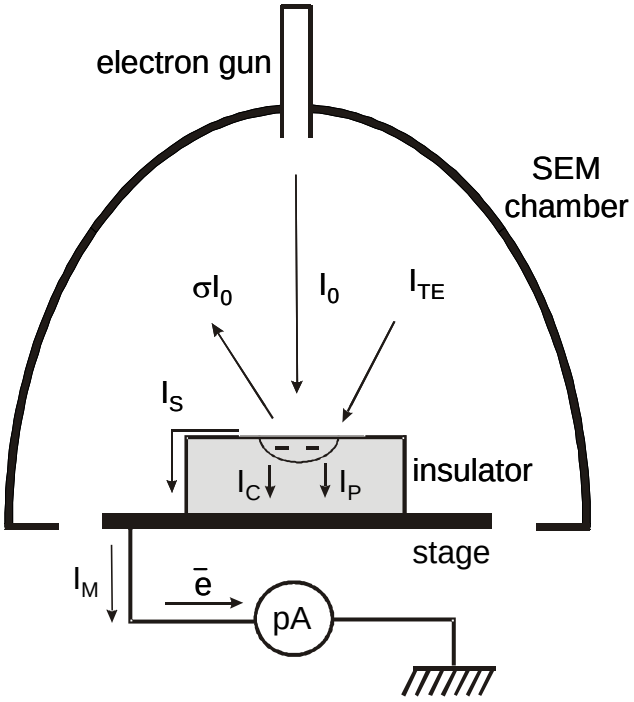

Figure 1, X. Meyza, J. Appl. Phys.

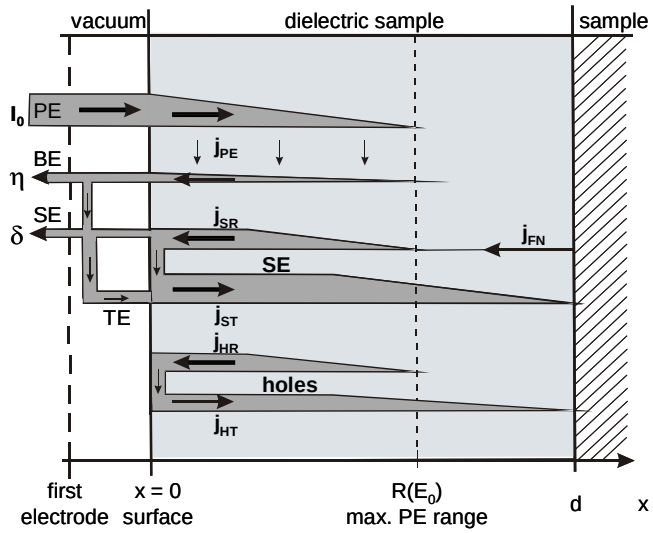

Figure 2, X. Meyza, J. Appl. Phys.

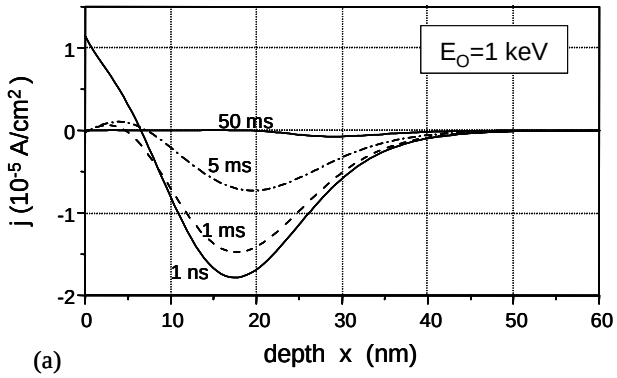

(a)

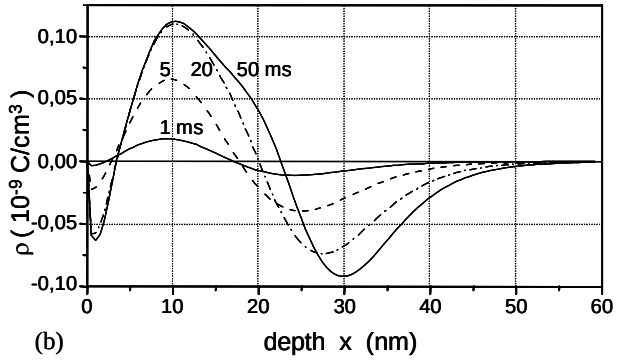

(b)

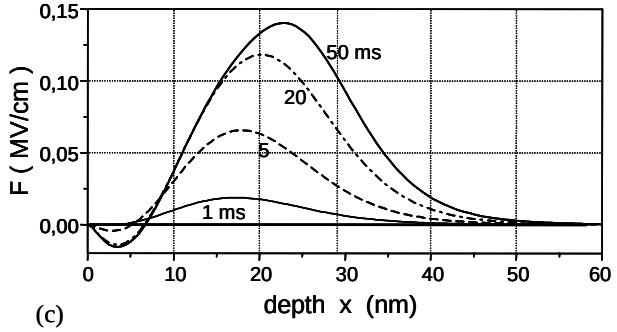

(c)

Figure 3, X. Meyza, J. Appl. Phys.

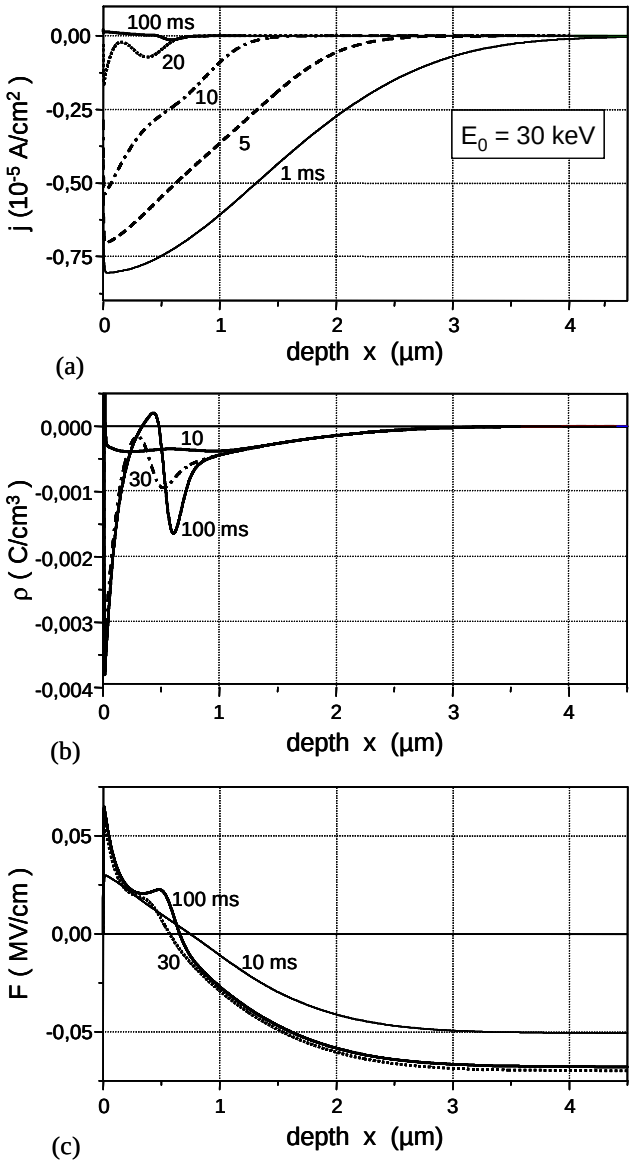

Figure 4, X. Meyza, J. Appl. Phys.

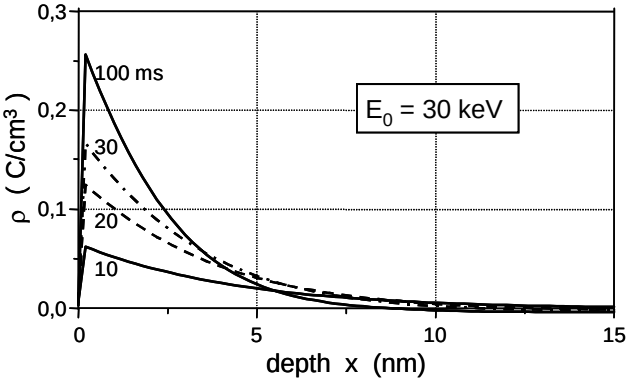

Figure 5, X. Meyza, J. Appl. Phys.

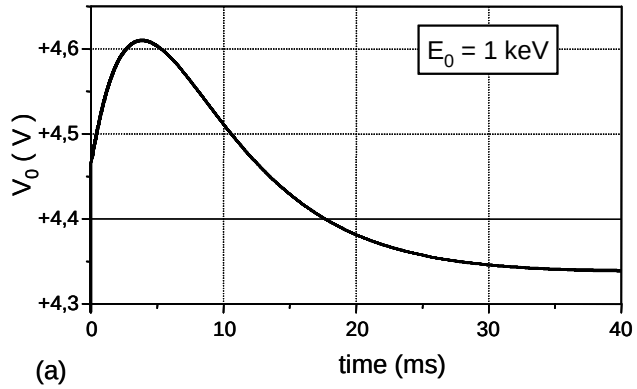

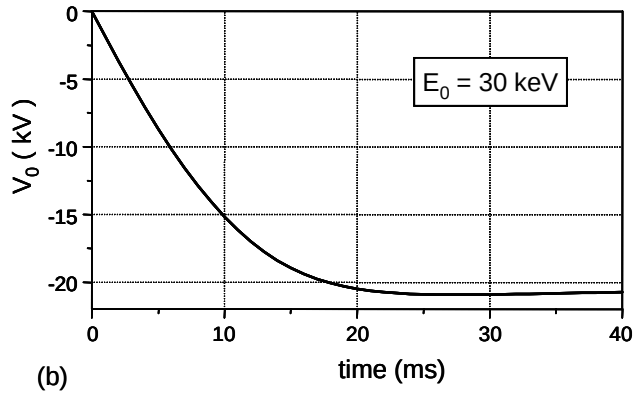

Figure 6, X. Meyza, J. Appl. Phys.

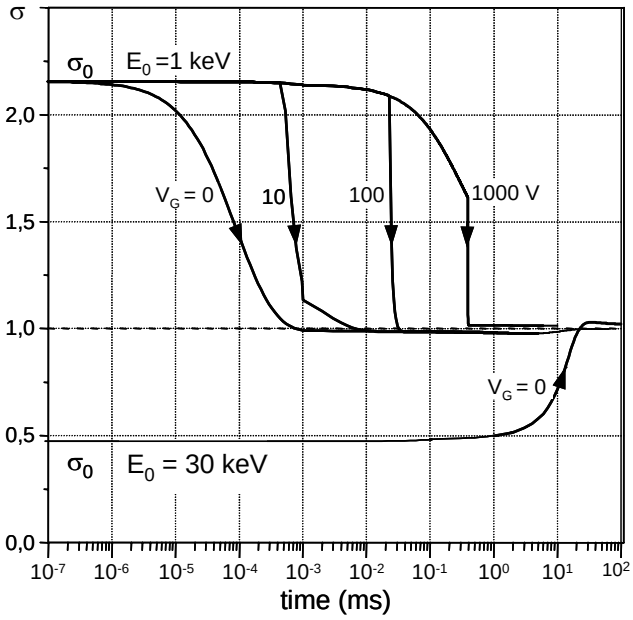

Figure 7, X. Meyza, J. Appl. Phys.

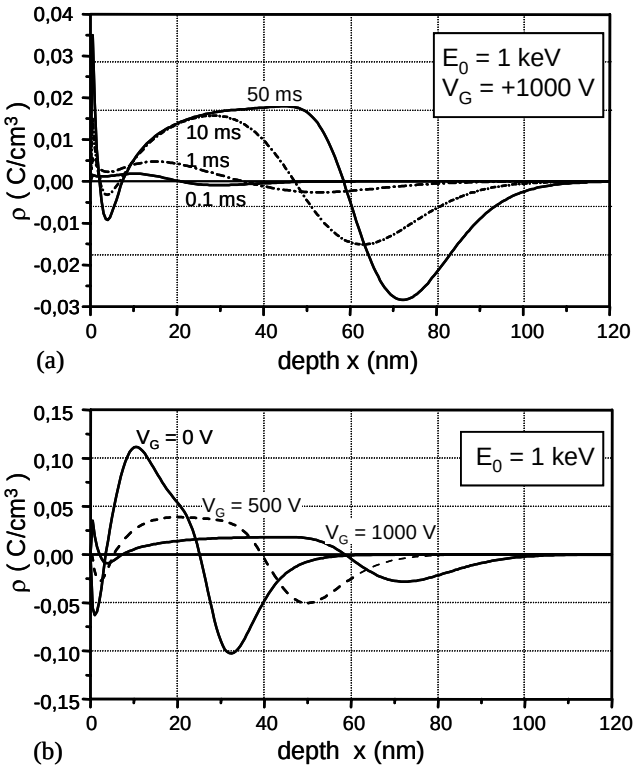

Figure 8, X. Meyza, J. Appl. Phys.

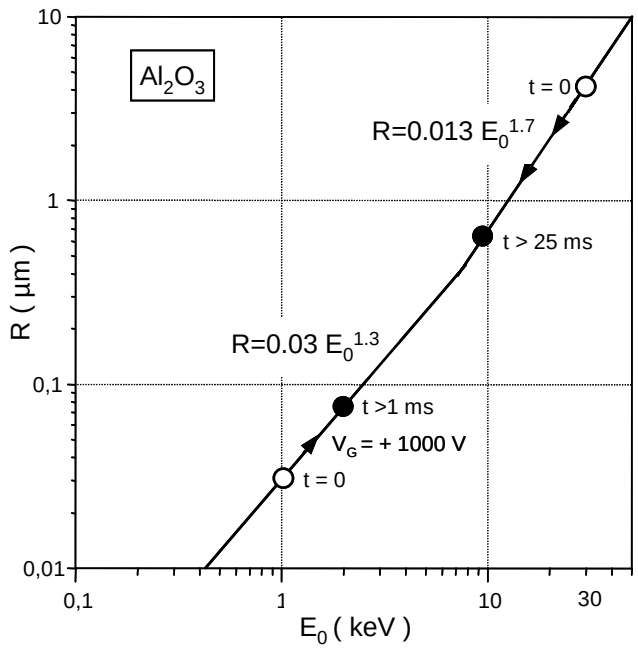

Figure 9, X. Meyza, J. Appl. Phys.

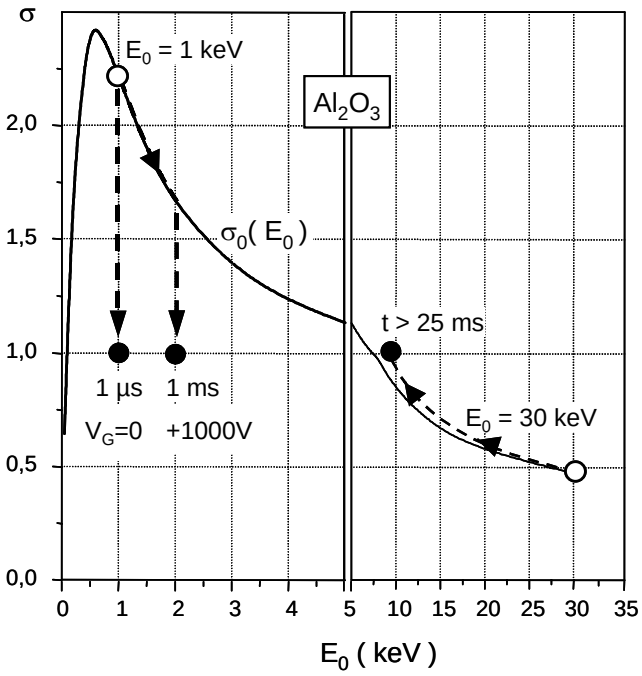

Figure 10, X. Meyza, J. Appl. Phys.

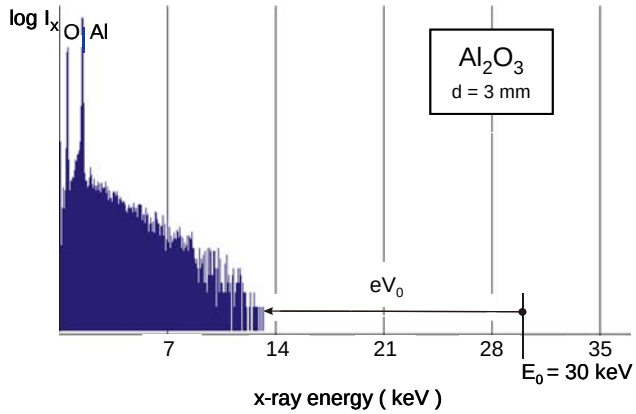

Figure 11, X. Meyza, J. Appl. Phys.

Figure 12, X. Meyza, J. Appl. Phys.